CrystEngComm

ROYAL SOCIETY OF CHEMISTRY

PAPER

View Article Online
View Journal | View Issue

Cite this: *CrystEngComm*, 2025, **27**, 5152

A simple low-temperature synthesis of fluorescent boron quantum dots for versatile applications†

Shutao Li,[a] Pengyi Ma,[a] Jinping Song,*[b] Xiaoting Guo,[a] Jianhua Xue[a] and Qi Ma *[b]

Received 17th June 2025,
Accepted 29th June 2025

DOI: 10.1039/d5ce00616c

rsc.li/crystengcomm

It is the first time to report the synthesis of small-molecule passivated boron quantum dots (BQDs) through a bottom-up strategy using L-cysteine (L-Cys) as a passivation agent and ammonium pentaborate tetrahydrate and boric acid as boron sources under a low reaction temperature of 100 °C. The morphology and surface structure of the prepared BQDs were characterized in detail using high-resolution transmission electron microscopy, X-ray photoelectron spectroscopy, Fourier-transform infrared spectroscopy, and X-ray diffraction. The as-obtained BQDs emitted blue fluorescence with a quantum yield of 1.14%, and the particle sizes are mainly distributed between 1.5 nm and 3.5 nm. Stability research results demonstrated that BQDs possess high stability performance. The findings revealed that BQDs could be used as a fluorescence nanoprobe for developing a fluorescence "turn-off/turn-on" sensing platform to detect the drug molecule sulfasalazine (SSZ) and Pb^{2+}. The proposed sensor indicates high sensitivity and selectivity towards SSZ, and the linear response range is 1–100 μmol L^{-1} with a detection limit of 0.9 μmol L^{-1}. The quenched fluorescence could be recovered by Pb^{2+} in the range of 40–180 μmol L^{-1} with a detection limit of 39.7 μmol L^{-1}. The proposed "turn off-turn on" sensor gives satisfactory results for practical sample analysis. Meanwhile, the thermodynamic data were estimated, and the corresponding quenching mechanisms were also discussed in detail. Moreover, BQDs had low cytotoxicity, which presented a potential application in cell imaging. They can also be used in the construction of LED and fluorescent film.

Introduction

Compared with semiconductor quantum dots and metal oxide quantum dots, non-metallic quantum dots present more advantages, such as low toxicity, good biocompatibility, cheap preparation cost and good chemical stability, and have displayed excellent application potential in various aspects including sensing, bioimaging, catalysis and light-emitting devices.[1–7] As a neighbor of the carbon element, not only is the atomic radius of the boron element very close to that of the carbon atom, but it also has similar sp^2 hybridization orbitals. More significantly, the electron-deficient properties of boron make its surface easily modify functional groups such as amino and carboxyl groups, facilitating binding with biomolecules (such as antibodies, DNA) or polymers, and expanding its applications in catalysis,[8] sensing,[9,10] tumour therapy and other fields.[11–14] Thus, in the past 5 years, researchers began to focus on boron quantum dots (BQDs). However, there are relatively few reports on the initial stage of BQD research.

At present, the preparation methods of BQDs can be divided into two types: top-down and bottom-up methods. Most of the literature reports the top-down method to prepare BQDs using bulk boron as the precursor. BQDs can be synthesized by ultrasonic exfoliation of boron powder[8,12,14,15] or solvothermal treatment of boron powder in organic phase media.[13] However, the strong bonding ability of bulk boron makes it difficult to synthesize high-quality BQDs on a large scale. Furthermore, nowadays, the reported BQDs are predominantly blue-fluorescent and have low quantum yields, greatly limiting their development and application. Regarding the bottom-up synthesis methods, boron-containing compounds are required as starting materials to achieve the conversion of boron-containing compounds into BQDs by chemical means. For example, Wang *et al.* used ammonium pentaborate and boric acid as precursors to obtain BQDs by hydrothermal polymerization and further reduction treatment under argon protection. This material can be combined with PVP to fabricate storage devices, exhibiting bistable electrical switching behaviour and non-volatile rewritable characteristics.[16] Compared to the top-down method, the bottom-up method has been reported relatively little. However, the advantages of this method are the wide variety of raw materials and the controllable design of surface structure and performance, which is very useful for developing boron quantum dots with multiple functions. Therefore, exploring more bottom-up

[a] *College of Chemistry and Chemical Engineering, Institute of Applied Chemistry, Shanxi Datong University, Datong, Shanxi, 037009, China*
[b] *Department of Chemistry, Xinzhou Normal University, Xinzhou, Shanxi, 034000, China. E-mail: songjphx@163.com, maqihx@163.com*

† Electronic supplementary information (ESI) available. See DOI: https://doi.org/10.1039/d5ce00616c

preparation methods, improving the stability and quantum yield of BQDs, and expanding the application areas will be the development trend of BQD nanomaterials.

Sulfasalazine (SSZ) as a typical sulfonamide antibiotic is widely used to treat autoimmune diseases such as ulcerative colitis, Crohn's disease, and rheumatoid arthritis.[17–19] SSZ can also inhibit the proliferation and metastasis of gastric cancer cells *in vitro*.[20] However, excessive use of SSZ can cause several adverse reactions such as severe allergies, dysfunction of the erythropoietin system, antibiotic resistance, or severe acute kidney injury.[21] At present, the methods for detecting SSZ include electrochemical methods,[22] high-performance liquid chromatography,[23] capillary electrophoresis mass spectrometry,[24] *etc.* These methods have the drawbacks of complex operation, high cost, and being long time-consuming, so the development of an efficient and convenient detection method has significant practical value.

With the rapid development of the chemical industry, wastewater and dust containing heavy metal Pb^{2+} ions are indiscriminately discharged into the environment, resulting in serious Pb^{2+} contamination of drinking water and other natural water resources in some areas. As one of the neurotoxic metals, Pb^{2+} is highly compatible with red blood cells and easily absorbed by the body, which can have adverse effects on human bones, brain, kidney, liver, central nervous system, cardiovascular system, and immune system.[25–27] Therefore, it is necessary to detect Pb^{2+} in water samples and the environment.[28] At present, several techniques including electrochemical method,[29] atomic fluorescence spectroscopy,[30] atomic absorption method,[31] inductively coupled plasma atomic emission spectroscopy,[32] and inductively coupled plasma mass spectrometry[33] have been applied to detect Pb^{2+} and also presented good response capability. However, there are no reports on the simultaneous detection of SSZ and Pb^{2+} through the fluorescence "turn-off/turn-on" sensing platform.

In this study, we synthesized blue-emitting BQDs by low-temperature reflux without inert gas protection using ammonium pentaborate and boric acid as boron precursors and L-cysteine as a reducing agent and surface passivating agent. This method avoids the high-temperature and high-pressure conditions in previous synthesis methods and is a safe, effective, and simple preparation method. Based on good fluorescence quenching of SSZ to BQDs *via* the sphere of action static quenching method and the good coordination ability of SSZ with Pb^{2+}, a fluorescence "turn-off/turn-on" sensing platform for detecting SSZ and Pb^{2+} was developed. In addition, the solid-state fluorescence characteristics and the corresponding applications were explored. The synthesis route and application diagram of BQDs are shown in Fig. 1.

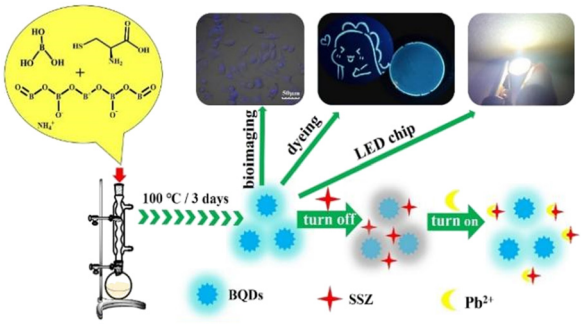

Fig. 1 Schematic diagram of the synthesis and application of blue fluorescent BQDs.

Experimental section

Reagents

Ammonium pentaborate tetrahydrate, L-cysteine (L-Cys), sulfamethazine (SMZ), (+)-rutin trihydrate, sulpiride, glutathione (GSH), *N*-acetyl-L-cysteine (NAC), mercaptosuccinic acid (MSA), sulfasalazine (SSZ) and quinine sulphate were purchased from Shanghai Aladdin Biochemistry Technology Co., Ltd. L-Tyrosine (L-Tyr), L-glutamic acid (L-Glu), L-serine (L-Ser), L-alanine (L-Ala), and cysteamine hydrochloride (Cystem·HCl) were purchased from Shanghai Macklin Biochemical Technology Co., Ltd. Boric acid was purchased from Hongyan Reagent Factory of Tianjin. Metal salts of analytical purity were purchased from the Tianjin Tianda Chemical Experimental Plant. Acetone was purchased from Tianjin Komeo Chemical Reagent Co., Ltd. SSZ enteric-coated tablets were bought from Shanghai Fuda Pharmaceutical Co., Ltd.

Instruments

UV-vis spectra were determined using a SPECORD 210 Plus instrument (Analytik Jena, Germany). A Cary Eclipse instrument (Varian, USA) was used to record the fluorescence spectra of BQDs. To test the particle size and the morphological characteristics of BQDs, a transmission electron microscope (JEM-2001F, JEOL, Japan) was used. Elemental composition was analyzed using an X-ray photoelectron spectrometer (Nexsa, Thermo Fisher Scientific, USA). Diffraction data of BQDs were collected using a SmartLab SE X-ray diffractometer (Rigaku, Japan). Infrared spectra were collected using a Fourier-transform infrared (FT-IR) instrument (Nicolet iS20, Thermo Fisher Scientific, USA). Fluorescence lifetime data were acquired using a steady-state instantaneous fluorescence spectrometer (PTI QuantaMaster 8000, HORIBA, Japan). Zeta potential was tested using a DelsaMax PRO analyzer (Beckman Coulter, USA). Cell imaging experiments were performed using an FV1200 confocal laser scanning microscope (Olympus, Japan).

Synthesis of BQDs

0.3 g of ammonium pentaborate tetrahydrate, 0.3 g of boric acid, and 0.1 g of L-Cys were dissolved in 15 mL of ultrapure water, then refluxed in an oil bath at 100 °C for 3 days. The products were slowly cooled to room temperature. 15 mL of acetone was added and the mixed solution was sealed to store in a refrigerator (4 °C) for 12 h. Subsequently, the mixture was centrifuged at 4000 rpm (RCF 2433*g*) for 10 min to remove the unreacted raw materials and some large particle substances. The supernatant was evaporated in a

rotation evaporator to remove all solvents; the obtained solid was redissolved with an appropriate amount of ultrapure water and further filtered with a 0.22 μm Millipore filter membrane. Finally, the filtrate was freeze-dried for 3 days to obtain a solid powder of brown-yellow BQDs, then sealed and stored for later use. The prepared BQD powder sample was dissolved in ultrapure water for further characterization and application.

Fluorescence quantum yield calculation

The relative quantum yields of the prepared BQDs were calculated according to the following formula using the quantum yield of quinine sulfate in 0.1 mol L^{-1} sulfuric acid solution as a reference.

$$\Phi_x = \Phi_{std} \frac{I_x}{A_x} \frac{A_{std}}{I_{std}} \frac{{\eta_x}^2}{{\eta_{std}}^2} \quad (1)$$

where Φ is the QY (fluorescence quantum yield) value of the fluorescent substance, I is the fluorescence integral area of the emission spectrum, A is the absorbance corresponding to the optimal excitation wavelength, η is the solvent refractive index, std denotes the reference substance quinine sulfate, and x denotes fluorescent BQDs. In the quantum yield measurement, the absorbance of all substances measured needs to be less than 0.10 at the excitation wavelength.

Fluorescence detection of SSZ and Pb^{2+}

0.0941 g of SSZ solid powder was dissolved in 500 μL of 1 mol L^{-1} NaOH solution, then diluted to 25 mL with ultrapure water to form a 0.1 mol L^{-1} stock solution, which was diluted into different concentrations of SSZ solution when used.

BQDs were directly dissolved in ultrapure water to form a stock solution of 0.3 mg mL^{-1} for further use. 20 μL of SSZ solution with different concentrations was added into 1980 μL of 0.3 mg mL^{-1} BQDs solution and shaken thoroughly; then the solution was incubated at room temperature for 10 min. The fluorescence data of the samples were measured under an excitation wavelength of 370 nm (the excitation and emission slits were both 10 nm). In the interference study, interference substance solutions were used instead of SSZ solution, and the fluorescence data were obtained under the same measurement conditions (the final concentration of the interference substance and SSZ was 50 μmol L^{-1}).

1.6560 g of $Pb(NO_3)_2$ was dissolved in 50 mL of ultrapure water to obtain a 0.1 mol L^{-1} $Pb(NO_3)_2$ stock solution for later use. 20 μL of Pb^{2+} solution with different concentrations was added to the 1980 μL BQDs–SSZ system (containing 0.3 mg mL^{-1} BQDs and 150 μmol L^{-1} SSZ) and allowed to stand for 5 min; then the mixture was gently shaken and continuously incubated for 60 min, followed by fluorescence measurement. In the interference study, the metal ion solution was used instead of Pb^{2+} solution, and the other operations were kept the same.

Real sample testing

SSZ enteric-coated tablets and laboratory tap water were used for the real sample analysis. The pretreatment process of enteric coated tablets is as follows: 0.7350 g of SSZ enteric-coated tablets were ground into powder, and 300 mg of the powder was dissolved in 500 μL of NaOH solution (1 mol L^{-1}) and further diluted to 500 mL with ultrapure water. The obtained solution was filtered with a 0.22 μm Millipore microporous filter to remove insoluble substances for later use. For the tap water sample, it was centrifuged at 4000 rpm for 10 min, then further filtered through a 0.22 μm Millipore microporous filter for later use. In the SSZ recovery experiment, 10 μL of real sample solution and 10 μL of ultrapure water (or 10 μL of SSZ standard solution with concentrations of 1, 5, and 10 mmol L^{-1}) were added to 1980 μL of BQDs solution (0.3 mg mL^{-1}) to react for 10 min, followed by the fluorescence measurement. For Pb^{2+} recovery experiments, 10 μL of real sample solution and 10 μL of ultrapure water (or 10 μL of Pb^{2+} standard solution with concentrations of 11, 16, and 20 mmol L^{-1}) were added to 1980 μL of the BQDs–SSZ system, and the mixture was incubated according to the previous protocol, followed by the corresponding fluorescence measurement. The recoveries and sample contents were further calculated. Each set of experiments was performed five times to minimize error.

Toxicity assessment and cell imaging research

MTT assay was carried out to evaluate the biotoxicity of BQDs. Human hepatocellular carcinoma cells (HepG2) were inoculated in 96-well plates and incubated for 24 h. Then the original medium was replaced with different concentrations of BQDs solution (25, 50, 100, 200 and 400 μg mL^{-1}) and incubated for 24 h, 48 h and 72 h, respectively. Subsequently, 10 μL of 5.0 mg mL^{-1} MTT solution was added to each well and incubated for another 4 h. The OD values were obtained by enzyme labelling measurements. Cell viability was evaluated as the ratio of the OD of cells treated with and without BQDs.

HepG2 cells were cultured in the original culture medium for 24 h, followed by further incubation with 100 μg mL^{-1} BQDs solution for 1 h. HepG2 cells were consecutively washed three times with PBS buffer solution, and then cell imaging was taken using a confocal microscope under excitation of 405 nm. To evaluate the recognition ability of the BQD nanoprobe for intracellular SSZ and Pb^{2+}, HepG2 cells incubated with BQDs solution were further incubated using 50 μmol L^{-1} SSZ solution for 2 h, then cell imaging experiments were performed under the same conditions. Similarly, HepG2 cells incubated with BQDs–SSZ solutions were further incubated using 100 μmol L^{-1} Pb^{2+} solution for 1 h, then used in cell imaging experiments.

Fabrication of fluorescent film and LED device, and fluorescence staining experiments

Fabrication of LED device: 1 g of BQDs solid powder was added to A/B glue with a mass ratio of 3 : 1 and stirred to obtain a uniform glue solution. This glue solution was spread

on a 395 nm LED chip to further cure at room temperature for 1 day.

Fluorescence staining experiment: non-fluorescent filter paper was uniformly stained using a Chinese brush dipped in BQDs solution (40 mg mL^{-1}), then dried at room temperature. The black cartoon template was placed on the above filter paper, then the optical photograph was taken under daylight and a 365 nm UV lamp.

Preparation of fluorescent film: 1 g of PVA powder was added to 10 mL of ultrapure water and stirred at 100 °C to dissolve completely. 2 mL of 10 mg mL^{-1} BQDs was added to 2 mL of PVA glue solution to mix uniformly until there were no bubbles. The mixed glue solution was spread onto a mold and further naturally dried for 2 days to get a flexible hydrogel film.

Results and discussion

Preparation and characterization

BQDs were synthesized using L-Cys as a passivation and chemical reduction agent and ammonium pentaborate tetrahydrate and boric acid as the boron sources *via* a bottom-up strategy. Compared with single top-down preparation methods, this method is safe, effective and simple to operate, which not only avoids using high-temperature and high-pressure conditions but also provides a new synthesis strategy. To acquire the best optical performance, various preparation conditions are optimized by adopting the single-factor variable method. As depicted in Table S1,† results showed that blue fluorescent BQDs could be obtained in the presence of L-Cys; there is no fluorescence in the absence of L-Cys, suggesting that L-Cys plays an important role in the formation of BQDs. The QY of the as-synthesized BQDs under optimal conditions (0.3 g of ammonium pentaborate tetrahydrate, 0.3 g of boric acid, 0.1 g of L-Cys, temperature of 100 °C, and the reaction time of 72 h) was estimated to be 1.14%. To explore the significant role of each functional group (–NH_2, –SH, –COOH) of the L-Cys in the synthesis of BQDs, four small molecules (including L-Ala, MSA, Cystem·HCl, and NAC) were chosen to replace L-Cys in the preparation process of BQDs. As shown in Fig. S1,† only the presence of Cystem·HCl could lead to slight fluorescence in the synthesis of BQDs; there is no obvious fluorescence in the presence of the other three small molecules, indicating that these three substances cannot convert boron sources into BQDs. Comparing the structure of these four small molecules and the corresponding fluorescence spectra (Fig. S1†), it is not difficult to find that BQDs cannot be formed when the small-molecule passivation agent contains only –COOH and –NH_2 (or –SH and –COOH) groups. When the small molecule contains –SH and –NH_2 groups, slight fluorescence confirms the formation of a small amount of BQDs. However, when the small molecule simultaneously contains three groups, it is more conducive to the transformation of the boron source to BQDs. In the conversion process from boron source to BQDs, the reducing property of –SH can reduce high-valent B to zero-valent B atoms, –NH_2 with lone pairs of electrons can easily form coordination bonds with B atoms possessing the empty orbitals. On the other hand, the carboxyl groups on the surface of BQDs can easily dissociate to make the BQDs negatively charged, which further stabilizes the BQDs.

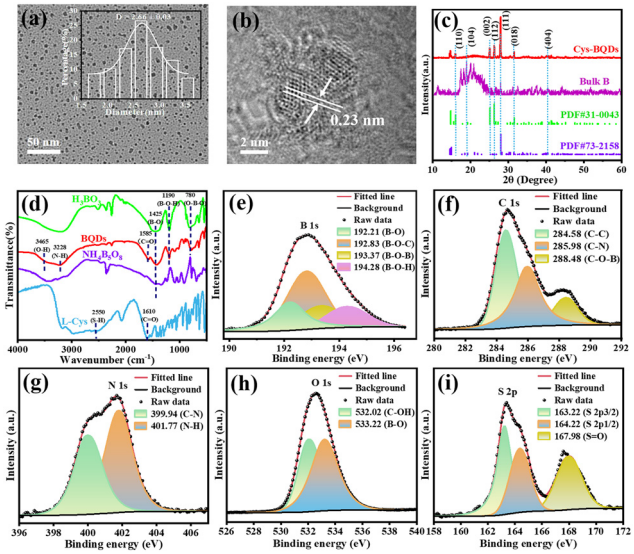

Fig. 2 (a) TEM image (the inset is the particle size distribution histograms), (b) high-resolution TEM image, (c) XRD, (d) FT-IR, and high-resolution (e) B 1s, (f) C 1s, (g) N 1s, (h) O 1s and (i) S 2p XPS spectra of BQDs.

The microstructure of BQDs was observed using a high-resolution TEM microscope. Fig. 2(a) clearly shows that the prepared BQDs are spherical particles without significant aggregation. The particle diameter was mainly distributed between 1.5 and 3.5 nm with an average particle size of 2.66 nm according to Nano Measure software fitting results, which follows the Gaussian model. Fig. 2(b) shows that BQDs have distinct lattice fringes with an interplanar distance of 0.23 nm, which is attributed to the (404) lattice planes of β-rhombohedral boron.[8] As depicted in Fig. 2(c), the diffraction peaks at 16.0°, 19.0°, 25.1°, 26.3°, 28.0°, 31.5° and 40.3° are assigned to the (110), (104), (002), (122), (111), (018) and (404) planes.[8,9,16] These diffraction peaks are enhanced in the BQDs, which is attributed to the existence of the structure of ammonium pentaborate and boric acid on the surface of BQDs. In addition, the broad diffraction peak located at 17.8°–23.8° is weakened in the XRD pattern of BQDs compared with bulk boron, which suggests that the bottom-up prepared BQDs possess different microstructural features from top-down derived BQDs.

In the FT-IR spectra of Fig. 2(d), the wide absorption bands at 3465 and 3228 cm^{-1} are attributed to the O–H/N–H stretching vibration,[34,35] indicating the presence of –OH and –NH_2. Compared with L-Cys, the shift of C=O stretching vibration from 1610 to 1585 cm^{-1} indicates that the passivator L-Cys on the surface of BQDs may form hydrogen bonding.[36,37] Meanwhile the disappearance of the –SH vibration peak at 2550 cm^{-1} may be due to the oxidation of L-Cys to cystine during the synthesis process.[35] The three characteristic peaks at 1425,

1190, and 780 cm^{-1} are attributed to B–O stretching vibration,[38,39] B–O–H bending vibration,[40,41] and O–B–O deformation vibration.[42,43] These data confirm that the surface of BQDs contains C═O, N–H, O–H, B–O–H, and O–B–O bonds.

Photoelectron spectroscopy was performed to characterize the composition of BQDs. The XPS full spectrum (Fig. S2 in the ESI†) clearly displays five peaks at 532.30, 400.87, 285.17, 192.19 and 163.93 eV, which are O 1s (47.29%), N 1s (8.28%), C 1s (29.24%), B 1s (11.21%), and S 2p (3.98%). Four peaks at 192.21, 192.83, 193.37 and 194.28 eV in the B 1s spectrum depicted in Fig. 2(e) correspond to B–O, B–O–C, B–O–B, and B–O–H bonds.[44] The C 1s spectrum in Fig. 2(f) shows three peaks at 284.58, 285.98, and 288.48 eV, which correspond to C–C, C–N, and C–O–B bonds, respectively.[45] Fig. 2(g) shows the N 1s spectra of BQDs; two peaks at 399.94 and 401.77 eV are ascribed to the C–N and N–H bonds.[46] In Fig. 2(h), the O 1s spectra of BQDs are resolved into two peaks at 532.02 and 533.22 eV, corresponding to C–OH (ref. 47) and B–O.[16,48] For the S 2p spectrum in Fig. 2(i), three peaks at 163.22, 164.22 and 167.98 eV originate from the S $2p_{3/2}$, S $2p_{1/2}$,[49–51] and S═O bonds.[47] XPS analysis results are consistent with the FT-IR results, indicating that hydrophilic groups such as hydroxyl, amino, and carboxyl groups exist on the surface of BQDs. These groups are mainly derived from the passivation agent on the surface of BQDs, which not only ensure the good water solubility of BQDs but also increase their stability.

Optical properties and stability of BQDs

The optical properties of BQDs are investigated by UV-vis absorption and fluorescence spectroscopy. As shown in Fig. 3(a), the aqueous solution of BQDs is yellowish under sunlight and emits blue fluorescence under the irradiation of a 365 nm UV lamp. The emission peak is located at 470 nm at the excitation of 370 nm. The UV-vis absorption spectrum shows that BQDs had a weak broad absorption peak at 280 nm, which is attributed to the n–π* transition of the C═O bond.[38] The bandgap width of ~5.28 eV (Fig. S3 in the ESI†) is significantly higher than the bandgap of BQDs obtained by the ammonium pentaborate and boric acid hydrothermal method reported in the literature (3.49 eV, the particle size is 6.4 nm).[16] It is well known that the bandgap width of the quantum dot would be larger as the quantum size decreases. In our research, the particle size of the as-synthesized BQDs is 2.53 nm, which is much smaller than 6.4 nm. As a result, it is reasonable to consider that the increased bandgap value is related to the quantum confinement effect. Such a large bandgap also indicates that the BQDs have low conductivity.

As can be seen from Fig. 3(b), the fluorescence intensity of BQDs increases and then decreases with the increase of the excitation wavelength accompanied by an obvious redshift of the emission peak position. This typical excitation dependence may be related to the surface defects and functional groups of BQDs.[52] Fig. 3(c) shows the dispersion of BQDs in eight solvents; it can be seen that BQDs are highly soluble in water, DMF, and DMSO solvents, slightly soluble in acetone, ethanol and acetonitrile, but completely insoluble in dichloromethane and cyclohexane. Overall, the solubility of BQDs enhances with the increase of solvent polarity. Moreover, the dispersed BQDs solution in these solvents emit blue fluorescence. Fig. 3(d) shows the normalized fluorescence spectra of BQDs in several solvents. It is noted that the maximum emission peak of BQDs in acetonitrile (medium polarity solvent) is located at 423 nm, which emerges as an obvious blueshift (~47 nm) compared with that in the stronger polar solvent of water. Although the polarity of ethanol solvent is between that of acetone and DMSO, the emission peak of BQDs in ethanol (467 nm) is higher than that in DMSO. It is considered to be due to the generation of hydrogen bonding between BQDs and ethanol, which has a more significant regulatory effect on the fluorescence spectrum than solvent polarity.[53]

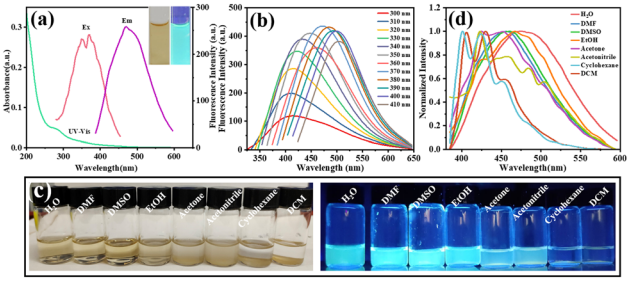

Fig. 3 (a) UV-vis absorption and fluorescence spectra of BQDs (inset is the corresponding optical photos). (b) Fluorescence emission spectra of BQDs at different excitation wavelengths, (c) optical photographs of BQDs in different solvents (left, under sunlight; right, under 365 nm UV light), (d) normalized fluorescence spectra of BQDs in different solvents.

The effects of pH, ion strength, UV exposure and storage time on the fluorescence intensity of BQDs were examined to investigate their optical stability (see Fig. S4 in the ESI†). It can be seen that the fluorescence intensity of BQDs is almost unaffected within a wide pH range of 2–12; this excellent fluorescence stability may be attributed to the presence of hydrophilic groups (–COOH and $–NH_2$) wrapped on the surface of BQDs.[54,55] BQDs possess good salt tolerance even in NaCl solution up to 2.0 M, which provides an opportunity for subsequent practical applications in cell imaging and physiological detection. The fluorescence intensity of the BQDs remained unchanged during storage for up to 15 days, indicating that BQDs had good storage stability. In addition, it is found that the fluorescence intensity of BQDs has no significant reduction even after 200 min of UV irradiation, demonstrating a good photobleaching resistance. This excellent optical stability will give a broad chance for its further application research.

Fluorescence "turn-off/turn-on" sensing platform based on BQDs for detection of SSZ and Pb^{2+}

The application potential of BQDs in the fluorescence sensing aspect was preferentially explored. Results show that the drug

molecule SSZ can bring about significant fluorescence quenching; the quenching effect of other molecules and ions are almost negligible (Fig. 4a), indicating that BQDs have excellent selective response ability for SSZ. From Fig. S5(a),† it is observed that the fluorescence intensity ratio values (F_0/F) of BQDs in the presence of SSZ are almost very close whether in water or in B–R buffer solution (pH 3–12). However, in the subsequent experiment, it was found that the fluorescence recovery ability of the BQDs–SSZ system upon the addition of Pb^{2+} is better in water than in B–R buffer solution. Thus, further sensing study was finally carried out in ultrapure water in view of the above consideration. From the dynamic fluorescence change curve of BQDs after the addition of SSZ in Fig. S5(b),† it can be observed that the fluorescence intensity of BQDs sharply decreases within 1 min upon the addition of SSZ and keeps unchanged in the following time, indicating that this sensor based on the BQD nanoprobe presents stable and fast response capacity for SSZ. To obtain a stable signal, 10 min of the reaction time was used in the following detection of SSZ.

Under the optimal detection conditions, the fluorescence intensity of BQDs decreases with the increase of SSZ concentration accompanied by the redshift of the emission peak from 470 nm to 496 nm (Fig. 4d). There is a good linear relationship between $\ln(F_0/F)$ and SSZ concentration (where F_0 and F are the fluorescence intensity of BQDs at 470 nm before and after adding SSZ), the linear equation is $\ln(F_0/F) = 0.0208 \cdot C + 0.03313$ ($R^2 = 0.998$), and the linear response range is 1–100 μmol L^{-1} (Fig. 4e). The lowest detection limit is 0.9 μmol L^{-1} according to IUPAC criteria (LOD = $3\sigma/K$).

We further explored whether the quenched fluorescence can be recovered. As shown in Fig. S6,† the addition of Pb^{2+} can effectively restore the fluorescence of the BQDs–SSZ system, meanwhile, the fluorescence spectral shape presents significant change, and obvious emission peaks emerge at 424, 461, 486 and 508 nm. These apparent changes imply that the BQDs–SSZ system has potential to develop a "turn-on" sensor for the detection of Pb^{2+}.

To evaluate the selectivity of BQDs–SSZ system for Pb^{2+}, the effects of other metal cations on the fluorescence recovery of the system were investigated. As shown in Fig. 4(d), the fluorescence recovery caused by Pb^{2+} is the most significant, while the other metal ions exhibit less fluorescence recovery for the BQDs–SSZ system. It can be seen that the "turn-on" fluorescence platform based on the BQDs–SSZ system has good selectivity for Pb^{2+}. Influences of the dosage of SSZ, pH, and the incubation time were further explored to achieve the best fluorescence recovery effect of the sensor. As shown in Fig. S7,† under the optimal experimental conditions (150 μmol L^{-1} SSZ concentration and 60 min of reaction time in ultrapure water), the best fluorescence recovery value can be obtained. Fig. 4(e) shows the fluorescence spectra of the BQDs–SSZ system before and after the addition of different concentrations of Pb^{2+}; the fluorescence intensity of the system increases in a gradient with the gradient increase of Pb^{2+} concentration. The fluorescence intensity recovery values at 486 nm ($F - F_0$, F_0 and F represent the fluorescence intensity of the BQDs–SSZ system before and after the addition of metal ions) show a good linear relationship with the Pb^{2+} concentration in the range of 40–180 μmol L^{-1}

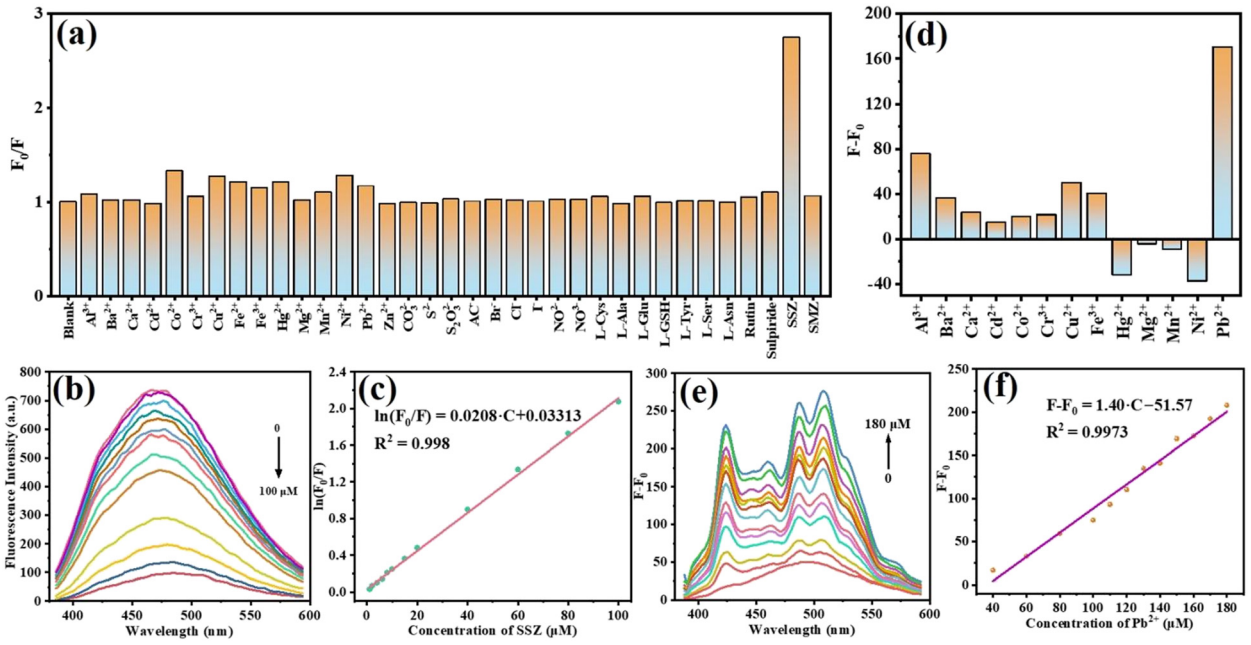

Fig. 4 (a) Fluorescence intensity ratios (F_0/F) of BQDs in the presence of different metal cations, anions, small molecules of amino acids, and drug molecules. (b) Fluorescence spectra of BQDs upon the addition of various concentrations of SSZ (from top to bottom: 0–100 μM). (c) Plot of $\ln(F_0/F)$ *versus* the concentration of SSZ. (d) Effect of different metal ions on fluorescence recovery of the BQDs–SSZ system. (e) Fluorescence spectra of BQDs in the presence of different concentrations of Pb^{2+} (from bottom to top: 0–180 μM). (f) Relationship between ($F - F_0$) and concentration of Pb^{2+} solution.

with a detection limit of 39.7 μmol L^{-1}; the fitted linear equation is $F - F_0 = 1.40 \cdot C - 51.57$ ($R^2 = 0.9973$) (Fig. 4f).

Quenching mechanism

The quenching mechanisms of BQDs by SSZ were studied in detail by various methods. From Fig. 5(a), no obvious overlap between the absorption spectra of SSZ and the emission spectra of BQDs indicated that there is no energy resonance transfer between them. The fluorescence decay curves in Fig. 5(b) and (c) show that the average fluorescence lifetimes of BQDs are 5.73 ns and 5.76 ns in the absence and presence of SSZ, suggesting that fluorescence quenching is a static quenching mechanism. At the same time, according to the Stern–Volmer formula (eqn (2)) of the bimolecular quenching process, the bimolecular quenching constant K_{SV} and the bimolecular quenching rate constant K_q at different temperatures were tested.

$$\frac{F_0}{F} = 1 + K_{SV}[Q] = K_q \tau_0 [Q] \quad (2)$$

F_0 and F represent the fluorescence intensity without and with SSZ, respectively, K_{SV} is the bimolecular quenching constant, K_q is the bimolecular quenching rate constant, τ_0 is the fluorescence lifetime, and [Q] is the actual concentration of SSZ. As shown in Fig. 5(d) and Table S2,† K_{SV} gradually decreases with the increase in temperature. K_q is 5.84×10^{12}–7.61×10^{12} L mol^{-1} s^{-1}, which is much larger than the maximum value of the diffusion collision quenching constant of 2.0×10^{10}. This further suggests that fluorescence quenching is a static quenching mechanism.[56] Theoretically, for a typical static quenching mechanism, a non-fluorescent complex would be formed; as a result, we should observe the additional spectral changes including the appearance (or disappearance) of an absorption peak and the shift of the peak position. However, it can be seen from Fig. 5(e) that the actual measured absorption spectra of the BQDs–SSZ system are completely overlapped with the theoretical superposition spectra of the absorption spectra of BQDs and SSZ, which means that the collision between BQDs and SSZ does not form a non-fluorescent complex. This phenomenon is similar to the sphere of action static quenching model.[57,58] In this special case, if the quencher appears near the fluorophore at the moment of excitation, a certain pre-quenching effect will occur before reaching steady state. That is to say, effective quenching occurs within a sphere with a radius greater than the sum of the radii of the fluorophore and the quencher molecules. All the above analyses show that the fluorescence quenching of BQDs by SSZ is mainly the sphere of action static quenching.

Based on the static quenching method, the binding sites and binding constants between SSZ and BQDs was further calculated by the static quenching double logarithm equation (eqn (3)).

$$\log\left[\frac{F_0 - F}{F}\right] = \log K_A + n \log[Q] \quad (3)$$

K_A is the binding constant, and n is the number of binding sites. As shown in Fig. 5(f) and Table S3,† the order of magnitude of the binding constants is above 10^4, indicating that there is a strong interaction between SSZ and BQDs. The binding site n is about 1, which confirms that there is only a single binding site between them. In addition, K_A decreases with the increase of temperature, which is consistent with the trend of K_{SV} changing with temperature, which further confirms the static quenching mechanism.[59]

The thermodynamic parameters of the interaction between BQDs and SSZ were determined by the van't Hoff equation (eqn (4)) and Gibbs free energy equation (eqn (5)), and the interaction mechanism and action force types were discussed.

$$\ln K_A = \frac{\Delta H}{RT} + \frac{\Delta S}{R} \quad (4)$$

$$\Delta G = \Delta H - T\Delta S \quad (5)$$

where ΔH, ΔS and ΔG are the standard enthalpy change, the standard entropy changes and the Gibbs free energy change of the reaction, respectively. As shown in Fig. 5(g) and Table S3,† ΔH and ΔS were calculated to be −85.2 kJ mol^{-1} and −194.24 J mol^{-1} K^{-1}; as a result, it is speculated that the interaction force between SSZ and BQDs should be hydrogen bonds or van der Waals forces. The presence of hydrogen bonds will reduce the fluorescence intensity of the system in the form of non-radiative relaxation.[60,61] Furthermore, $\Delta G < 0$ also implies that the static quenching is a spontaneous exothermic process.[62] The zeta potential in Fig. 5(h) displays

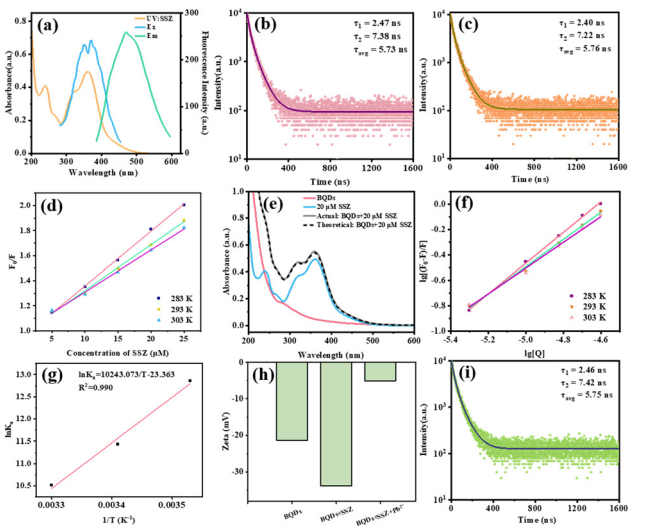

Fig. 5 (a) Excitation and emission spectra of BQDs and UV absorption spectra of SSZ. (b) The fluorescence-decay curves of BQDs. (c) The fluorescence-decay curves of BQDs–SSZ. (d) Stern–Volmer curves of BQDs–SSZ at different temperatures. (e) UV-vis absorption spectra of BQDs, SSZ, and BQDs + SSZ. (f) Double logarithmic plots of BQDs–SSZ binding at different temperatures. (g) Van't Hoff curves of BQDs–SSZ binding. (h) Zeta potential of BQDs, BQDs + SSZ, and BQDs + SSZ + Pb^{2+}. (i) Fluorescence attenuation curves of BQDs–SSZ–Pb^{2+}.

that BQDs are negatively charged, which is attributed to the partially dissociated carboxyl group on the surface of BQDs. When SSZ is added, the negative charge of the BQDs–SSZ system increases. On the one hand, the partial carboxyl group or hydroxyl group of the SSZ molecule will form hydrogen bonds with the carboxyl groups on the surface of BQDs, on the other hand, the partial free functional groups of SSZ are also prone to deprotonate, leading to the increase of the negative charge. However, it is not hard to find that the negative charge of the BQDs–SSZ–Pb^{2+} ternary system is obviously less than that of the BQDs or BQDs–SSZ binary system. The main reason is that the presence of Pb^{2+} not only makes SSZ move away from the surroundings of BQDs but also the partial positively charged Pb^{2+} will move close to BQDs, finally leading to a reduction in the negative charge of the system. Furthermore, the fluorescence lifetime of the BQDs–SSZ–Pb^{2+} system is 5.75 ns, which is consistent with the fluorescence lifetime of BQDs and the BQDs–SSZ system, implying that Pb^{2+} forms a complex with SSZ. This can further prevent the collision interaction between SSZ and BQDs (Fig. 5i).

Practical sample analysis

Tables S4 and S5† show the analysis result in SSZ enteric-coated tablets and laboratory tap water practical samples, respectively. As can be seen from Table S4,† the recovery rate of SSZ is between 96.4% and 106.88%, and the RSD is between 0.37% and 1.91% (n = 5). The concentration of SSZ in the measured solution is determined to be 5.47 μmol L^{-1}. According to this, the measured content of SSZ in each tablet is calculated to be 0.267 g per tablet, which is consistent with the theoretical value of 0.250 g per tablet in drug specifications. As shown in Table S5,† Pb^{2+} is not detected in tap water samples, and the recovery rate of the BQDs–SSZ sensing platform for the determination of Pb^{2+} is 106.01–108.15% with RSDs in the range of 0.91–5.04% (n = 5). Satisfactory experimental results indicate that the proposed fluorescence "turn-off/turn-on" sensing platform is feasible and reliable for the detection of SSZ and Pb^{2+}.

Cell bioimaging research

Fig. 6(a) shows the cell survival histogram of HepG2 cells after incubating in BQD solutions with different concentrations for 24, 48 and 72 h. It is found that the survival rate of HepG2 cells in 400 μg mL^{-1} BQDs still exceeds 80% after incubating for 72 h. This demonstrates that BQDs have low cytotoxicity. From the confocal images of HepG2 cells depicted in Fig. 6(b), obvious blue fluorescence can be observed in the cell membrane and cytoplasm, indicating that BQD nanoprobes can penetrate the cell membrane and

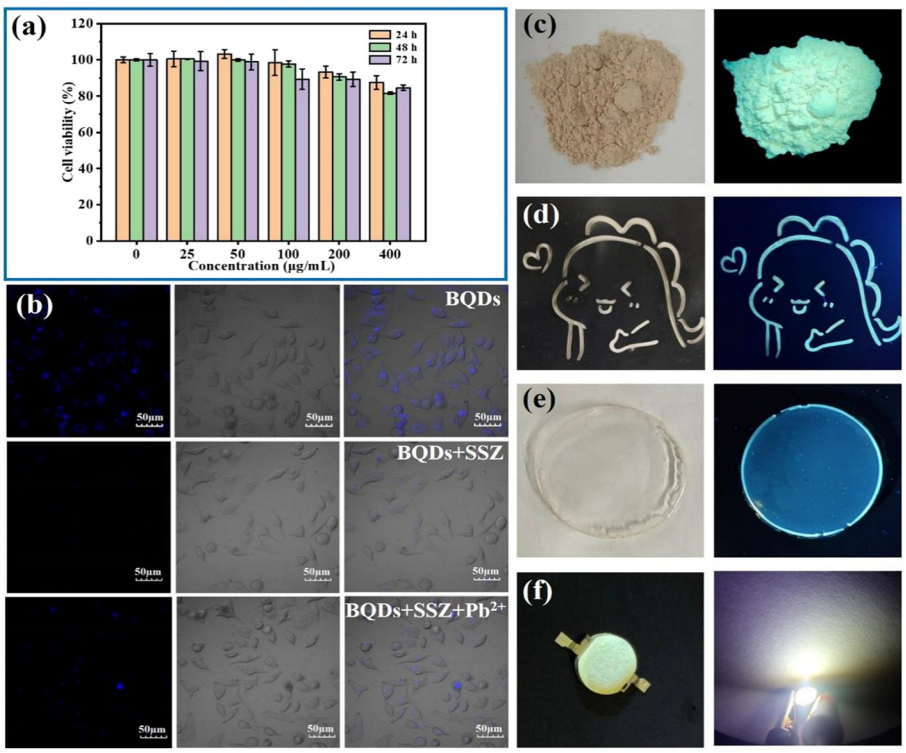

Fig. 6 (a) Cell survival histogram of HepG2 cells after incubating in BQDs solutions with different concentrations for 24, 48 and 72 h. (b) Confocal images of HepG2 cells after incubation for 1 h in 100 μg mL^{-1} BQDs solution. Confocal image of HepG2 cells after incubation for 1 h in BQDs solution, followed by 2 h incubation with 50 μmol L^{-1} SSZ. Confocal images of HepG2 cells incubated in BQDs for 1 h, 50 μmol L^{-1} SSZ for 2 h, and then in 100 μmol L^{-1} Pb^{2+} for 1 h. (c) BQDs powder diagram under sunlight (left) and ultraviolet lamp (right). (d) Fluorescence staining pattern under sunlight (left) and ultraviolet lamp (right). (e) BQDs/PVA film under sunlight (left) and ultraviolet light (right). (f) LED (light-emitting device).

enter the cytoplasmic region for biological staining. Subsequently, HepG2 cells stained by BQDs were further incubated with 50 μmol L^{-1} SSZ for 2 h; it is noted that the blue fluorescence inside the cells is weakened, which implies that SSZ can enter the cells to react with BQDs inside the cells. However, once Pb^{2+} was further added to incubate for 1 h, the weakened fluorescence can be recovered. All these phenomena show that BQDs can recognize intracellular SSZ and Pb^{2+}, which will have potential application in bioimaging study.

Applications in LED devices, fluorescence staining and luminescent film

As depicted in Fig. 6(c), BQDs powder is earthy yellow under sunlight and exhibits light yellow fluorescence under a 365 nm UV lamp. A cartoon pattern stained with BQD inks presents the natural color of the filter paper under sunlight and shows clear blue fluorescence under a 365 nm UV lamp (Fig. 6d). Similarly, the prepared BQDs/PVA films also exhibit blue fluorescence (Fig. 6e). Moreover, LED devices constructed with BQDs can emit bright warm yellow light sources (Fig. 6f). These data display that BQDs have good solid-state fluorescence characteristics. In order to better understand the stability in solid-state fluorescence applications of BQDs, we conducted relevant tests on the fluorescence quantum yield of PVA film and solid powder. As shown in Fig. S5,† the fluorescence quantum yield values of BQDs solid powder and BQDs/PVA fluorescent film were measured to be 0.89% and 4.91%, respectively. In contrast, the QY of BQDs solid powder is relatively close to that of BQDs aqueous solution (1.1%). However, the enhancement of fluorescence quantum yield from solution to PVA film may be a result of the lower reabsorption derived from larger Stokes shift, enhanced surface passivation of BQDs in a more enclosed environment of the optical coating substrate, dielectric confinement effect, and instrument calibration error. It verifies that the fluorescence of BQDs is stable in solid-state applications.

Conclusions

In summary, blue-emitting BQDs were synthesized through a bottom-up approach using ammonium pentaborate and boric acid as boron sources and L-cysteine as a reducing agent and surface passivator under the condition of low-temperature reflux without gas protection. This method avoids high-temperature and high-pressure conditions and has the advantages of being safe and simple to operate. The structure and morphology of as-synthesized BQDs were characterized using various techniques. In view of the excellent optical performance and stability, BQDs were successfully used for fluorescent "turn off-turn on" detection of SSZ and Pb^{2+} with detection limits of 0.9 μmol L^{-1} and 39.7 μmol L^{-1}, respectively. The recovery rate of SSZ and Pb^{2+} in the practical sample analysis is 96.4–106.88% and 106.01–108.15%, respectively. Furthermore, results showed that BQDs could also be used in cell imaging and the construction of LED and fluorescent film. This research provides a new preparation thought for QDs, which will also further expand the application of BQDs.

Data availability

All data generated or analyzed during this study are included in this published article and its ESI† files.

Author contributions

Shutao Li designed the experiments, analyzed data, and wrote the manuscript. PengYi Ma, Xiaoting Guo, and Jianhua Xue performed all experiments associated with synthesis, fluorescence properties, cell image, and mechanistic studies. Jinping Song and Qi Ma provided supervision, funding, and ideation to writing the manuscript.

Conflicts of interest

There are no conflicts to declare.

References

1 A. Kumar, I. Kumar, S. Kumar, A. Sharma, A. Sharma and A. K. Gathania, *Carbon Lett.*, 2025, 1–16.
2 G. Paramasivam, V. V. Palem, S. Meenakshy, L. K. Suresh, M. Gangopadhyay, S. Antherjanam and A. K. Sundramoorthy, *Colloids Surf., B*, 2024, **241**, 114032.
3 A. Kumar, I. Kumar and A. K. Gathania, *Sci. Rep.*, 2022, **12**, 22495.
4 R. Atchudan, S. Perumal, S. C. Kishore, A. K. Sundramoorthy, D. Manoj, S. Sambasivam, R. S. Kumar, M. Alagan, S. Ramalingam, S. W. Lee and Y. R. Lee, *J. Taiwan Inst. Chem. Eng.*, 2024, **165**, 105770.
5 R. Jerome and A. K. Sundramoorthy, *J. Electrochem. Soc.*, 2019, **166**, B3017–B3024.
6 G. Sridharan, C. J. T. Godwin, R. Atchudan, S. Arya, M. Govindasamy, S. M. Osman and A. K. Sundramoorthy, *J. Taiwan Inst. Chem. Eng.*, 2024, **163**, 105320.
7 J. Rajendran, A. N. Reshetilov and A. K. Sundramoorthy, *RSC Adv.*, 2021, **11**, 3445–3451.
8 M. Yang, H. Jin and R. Gui, *ACS Appl. Mater. Interfaces*, 2022, **14**, 56986–56997.
9 D. J. Joshi, S. Jha, N. I. Malek, T. J. Park and S. K. Kailasa, *Spectrochim. Acta, Part A*, 2025, **326**, 125232.
10 M. Yang, H. Jin, Z. Sun and R. Gui, *J. Mater. Chem. A*, 2022, **10**, 5111–5146.
11 C. Wang, Q. Chen, H. Chen, J. Liu, Y. Song, J. Liu, D. Li, Y. Ge, Y. Gong, Y. Zhang and H. Zhang, *Opto-Electron. Adv.*, 2021, **4**, 200032.
12 J. Hao, G. Tai, J. Zhou, R. Wang, C. Hou and W. Guo, *ACS Appl. Mater. Interfaces*, 2020, **12**, 17669–17675.
13 T. Guo, Q. Tang, Y. Guo, H. Qiu, J. Dai, C. Xing, S. Zhuang and G. Huang, *ACS Appl. Mater. Interfaces*, 2020, **13**, 306–311.
14 L. Wang, S. M. Xu, S. Guan, X. Qu, G. I. N. Waterhouse, S. He and S. Zhou, *J. Mater. Chem. B*, 2020, **8**, 9881–9887.

15 M. Yang, H. Jin and R. Gui, *J. Colloid Interface Sci.*, 2023, **639**, 49–58.
16 H. Wang, J. Han, M. Wang, L. Wang, S. Jia, H. Cao, S. Hu and Y. B. He, *CrystEngComm*, 2022, **24**, 3469–3474.
17 A. Soltani, V. Erfani Moghadam, A. Yahyazadeh and N. O. Mahmoodi, *J. Mol. Struct.*, 2022, **1267**, 133568.
18 A. T. Fiori-Duarte, R. E. F. de Paiva, C. M. Manzano, W. R. Lustri and P. P. Corbi, *J. Mol. Struct.*, 2020, **1214**, 128158.
19 N. Rahman and N. Khalil, *Spectrochim. Acta, Part A*, 2023, **300**, 122865.
20 J. Zhuang, X. Liu, Y. Yang, Y. Zhang and G. Guan, *J. Cell. Mol. Med.*, 2021, **25**, 5372–5380.
21 M. Durando, H. Tiu and J. S. Kim, *Am. J. Kidney Dis.*, 2017, **70**, 869–873.
22 H. Beitollahi and R. Yoonesfar, *Inorg. Nano-Met. Chem.*, 2017, **47**, 1441–1448.
23 G. Z. Gu, H. M. Xia, Z. Q. Pang, Z. Y. Liu, X. G. Jiang and J. Chen, *J. Chromatogr., B*, 2011, **879**, 449–456.
24 G. Font, A. Juan-García and Y. Picó, *J. Chromatogr. A*, 2007, **1159**, 233–241.
25 D. Wu, Y. Hu, H. Cheng and X. Ye, *Molecules*, 2023, **28**, 3601.
26 G. Liang, Y. Man, A. Li, X. Jin, X. Liu and L. Pan, *Microchem. J.*, 2017, **131**, 145–153.
27 Y. Kim and J. Kim, *Opt. Mater.*, 2020, **99**, 109514.
28 G. Wang, L. T. Chu, H. Hartanto, W. B. Utomo, R. A. Pravasta and T. H. Chen, *ACS Sens.*, 2019, **5**, 19–23.
29 K. Koirala, J. H. Santos, A. L. Tan, M. A. Ali and A. H. Mirza, *Sens. Rev.*, 2016, **36**, 339–346.
30 Z. Wan, Z. Xu and J. Wang, *Analyst*, 2006, **131**, 141–147.
31 R. A. Zounr, M. Tuzen and M. Y. Khuhawar, *J. Mol. Liq.*, 2018, **259**, 220–226.
32 C. D. B. Amaral, D. Schiavo, J. A. V. A. Barros, R. C. Machado, A. R. A. Nogueira and J. A. Nóbrega, *Anal. Lett.*, 2016, **49**, 2092–2098.
33 A. Cocherie and M. Robert, *Chem. Geol.*, 2007, **243**, 90–104.
34 Y. Wang, F. Zeng, L. Zhang, G. Chen, Q. Zhang, N. Zhang and W. Zhang, *Diamond Relat. Mater.*, 2023, **139**, 110343.
35 J. Zhang, D. Nan, S. Pan, H. Liu, H. Yang and X. Hu, *Spectrochim. Acta, Part A*, 2019, **221**, 117161.
36 J. Binoy, N. B. Prathima, C. Murali Krishna, C. Santhosh, I. Hubert Joe and V. S. Jayakumar, *Laser Phys.*, 2006, **16**, 1253–1263.
37 N. V. Aralikatti, *J. Mol. Struct.*, 2018, **1173**, 814–821.
38 S. N. Karadag, O. Ustun, A. Yilmaz and M. Yilmaz, *Chem. Phys.*, 2022, **562**, 111678.
39 Z. Liu, Z. Mo, X. Niu, X. Yang, Y. Jiang, P. Zhao, N. Liu and R. Guo, *J. Colloid Interface Sci.*, 2020, **566**, 357–368.
40 M. Masteri-Farahani, F. Ghorbani and N. Mosleh, *Spectrochim. Acta, Part A*, 2021, **245**, 118892.
41 W. Zeng, D. Huang, G. Zhu, B. Lv and Y. Yi, *Anal. Sci.*, 2020, **36**, 1203–1207.
42 S. Zhou, T. Xu, F. Jiang, N. Song, L. Shi and P. Ding, *J. Mater. Chem. C*, 2019, **7**, 13896–13903.
43 L. Wang, J. Jana, J. S. Chung and S. H. Hur, *Spectrochim. Acta, Part A*, 2021, **260**, 119895.
44 X. Zhang, Y. Zhao, S. Wang and X. Jing, *Mater. Chem. Front.*, 2021, **5**, 5534–5548.
45 Q. Yao, Y. Feng, M. Rong, S. He and X. Chen, *Microchim. Acta*, 2017, **184**, 4217–4223.
46 X. Tang, Y. Zhao, H. Yu, S. Cui, H. Temple, E. Amador, Y. Gao, M. Chen, S. Wang, Z. Hu and W. Chen, *Mater. Today Adv.*, 2023, **18**, 100383.
47 S. Riaz and S. J. Park, *J. Ind. Eng. Chem.*, 2022, **105**, 111–120.
48 L. Li, F. Ma, C. Jia, Q. Li, X. He, J. Sun, R. Jiang, Z. Lei and Z. H. Liu, *Adv. Sci.*, 2023, **10**, 2301682.
49 P. M. Shanthi, P. J. Hanumantha, K. Ramalinga, B. Gattu, M. K. Datta and P. N. Kumta, *J. Electrochem.*, 2019, **166**, A1827–A1835.
50 V. Secchi, S. Franchi, M. Santi, M. Dettin, A. Zamuner, G. Iucci and C. Battocchio, *J. Phys. Chem. C*, 2018, **122**, 6236–6239.
51 J. A. Syed, S. A. Sardar, S. Yagi and K. Tanaka, *Surf. Sci.*, 2004, **566–568**, 597–602.
52 J. Wan, X. Zhang, Y. Jiang, S. Xu, J. Li, M. Yu, K. Zhang and Z. Su, *J. Mater. Chem. B*, 2022, **10**, 6991–7002.
53 X. Ren, L. Guan, W. Shi, J. Zhang, M. Chen, T. Luo, C. Liu, Y. Lan, Z. Chen, X. Chen and X. Li, *J. Mol. Liq.*, 2024, **403**, 124872.
54 X. Jia, J. Li and E. Wang, *Nanoscale*, 2012, **4**, 5572–5575.
55 A. O. da Silva, M. O. Rodrigues, M. H. Sousa and A. F. C. Campos, *Colloids Surf., A*, 2021, **621**, 126578.
56 I. Vinçon, A. Barfüßer, J. Feldmann and Q. A. Akkerman, *J. Am. Chem. Soc.*, 2023, **145**, 14395–14403.
57 A. Safarnejad, M. Shaghaghi, G. Dehghan and S. Soltani, *J. Lumin.*, 2016, **176**, 149–158.
58 A. A. Aboalhassan, S. A. El Daly, E. Z. M. Ebeid and M. A. S. Sakr, *J. Fluoresc.*, 2022, **32**, 2257–2269.
59 T. W. Cao, X. P. Tan, L. P. Huang, J. W. Shi and G. Xu, *Fenxi Huaxue*, 2019, **47**, e19027–e19033.
60 Q. Gong, Y. Li, H. Wang, G. Wang, Q. Feng, Y. Zhong and F. Liu, *J. Phys. Chem. C*, 2022, **126**, 18429–18438.
61 P. Salehian, B. Shareghi and M. Hosseini-Koupaei, *J. Biol. Phys.*, 2019, **45**, 89–106.
62 W. Wang, Q. Zhang, X. Xiong, Y. Zheng, W. Yang and L. Du, *J. Mol. Liq.*, 2020, **316**, 1138770.